PASJ: Publ. Astron. Soc. Japan **61**, 375–385, 2009 April 25

North Ecliptic Pole Wide Field Survey of AKARI: Survey Strategy and Data Characteristics

Hyung Mok LEE,[1] Seong Jin KIM,[1] Myungshin IM,[1] Hideo MATSUHARA,[2] Shinki OYABU,[2] Takehiko WADA,[2] Takao NAKAGAWA,[2] Jongwan KO,[1] Hyun Jin SHIM,[1] Myung Gyoon LEE,[1] Narae HWANG,[1] Toshinobu TAKAGI,[2] and Chris PEARSON[2]

[1]*Astronomy Program, FPRD, Department of Physics and Astronomy, Seoul National University, Shillim-Dong, Kwanak-Gu, Seoul 151-742, South Korea*
hmlee@snu.ac.kr

[2]*Institute of Space and Astronautical Science, Japan Aerospace Exploration Agency, Yoshinodai 3-1-1, Sagamihara, Kanagawa 229-8510*

(Received 2008 May 31; accepted 2008 December 5)

Abstract

We present the survey strategy and the data characteristics of the North Ecliptic Pole (NEP) Wide Survey of AKARI. The survey was carried out for about one year starting from 2006 May with 9 passbands from 2.5 to 24 μm and the areal coverage of about 5.8 degree^2 centered on NEP. The survey depth reaches to 21.8 AB magnitude near infrared (NIR) bands, and $\sim$18.6 AB magnitude at the mid infrared (MIR) bands such as 15 and 18 μm. The total number of sources detected in this survey is about 104000, with more sources in NIR than in the MIR. We have cross matched infrared sources with optically identified sources in CFHT imaging survey which covered about 2 degree^2 within NEP-Wide survey region in order to characterize the nature of infrared sources. The majority of the MIR sources at 15 and 18 μm bands are found to be star forming disk galaxies, with smaller fraction of early type galaxies and AGNs. We found that a large fraction (60%–80%) of bright sources in 9 and 11 μm is stars while stellar fraction decreases toward fainter sources. We present the histograms of the sources at MIR bands at 9, 11, 15, and 18 μm. The number of sources per magnitude thus varies as $m^{0.6}$ for longer wavelength sources while shorter wavelength sources show steeper variation with m, where m is the AB magnitude.

Key words: infrared: galaxies — photometry

1. Introduction

AKARI (Murakami et al. 2007), an infrared space telescope, was launched on 2006 February 21 (UT) and has successfully carried out its missions including all sky surveys at mid to far infrared wavelengths and pointed observations at near to far infared. The 'cold' mission lasted until the helium boil out on 2007 August 26.

In addition to the all sky surveys, AKARI has devoted large amount of observational time to cover the North Ecliptic Pole (NEP) area since the NEP [and the South Ecliptic Pole (SEP) as well] is the only location in the sky with excellent visibility for polar sun synchronous orbit missions like AKARI. The NEP survey of AKARI is composed of two programs: Deep (NEP-Deep) and Wide (NEP-Wide) surveys (Matsuhara et al. 2006). The NEP-Wide observed a large area ($\approx$5.8 degree^2), while the NEP-Deep covered a smaller (0.38 degree^2) area with integration times longer than the NEP-Wide survey by a factor of 3–10. These two surveys are intended to be mutually complementary.

Both NEP-Wide and NEP-Deep surveys are done with all the filters of InfraRed Camera (IRC) covering near to mid infrared wavelengths (see Onaka et al. 2007, for the description of this instrument). The IRC wide bands are designated as *N2*, *N3*, *N4*, *S7*, *S9W*, *S11*, *L15*, *L18W*, *L24*. The numbers appearing after the roman alphabet represent the approximate effective wavelengths in units of μm, while the *W*'s for 9 and 18 μm represent the fact that the bandwidths are wider.

Prior to the full scale survey of the NEP, mini-surveys were carried out during the performance verification period in order to check the performance of the instruments as well as survey strategies. The results of such surveys were already published (Lee et al. 2007; Matsuhara et al. 2007). In addition, AKARI has regularly observed the 'monitor field' near NEP centered at $\alpha = 17^{\rm h}55^{\rm m}24^{\rm s}$, $\delta = 66°37'32''$ with all 9 IRC bands in order to check the stability of the instruments during the entire period of the NEP Surveys. The preliminary analysis of the monitor field data was presented by Takagi et al. (2007).

The NEP-Wide data set has similar but slightly worse (by up to $0.^{\rm m}6$) sensitivity compared to that of the early data of NEP-Deep as presented by Lee et al. (2007) who focused on the nature of 11 μm selected sources covering around $10' \times 10'$ field of view (FOV). They found that a majority of sources detected at mid infrared (MIR) are star forming galaxies located at redshift of $0.2 < z < 0.7$. Some of the sources are suspected to be very red objects at much higher redshift. Since the observed area was much smaller than the entire NEP-Wide, there were only 72 sources with 11 μm magnitude brighter than 18.5. By simple scaling, we expect to detect around 15000 sources in the entire NEP-Wide area with a similar flux limit.

The optical data are very useful in identifying the sources detected by AKARI since they provide high resolution images. The optical survey was carried out before the launch of AKARI covering about 2 degree^2 inside NEP-Wide survey area with the

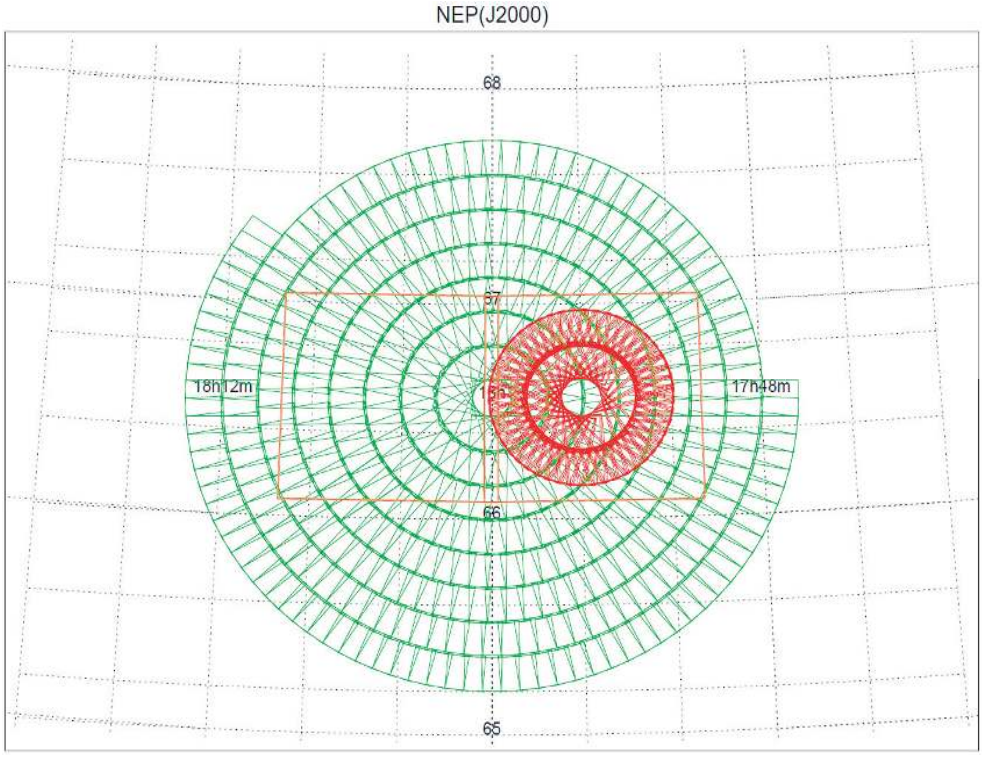

Fig. 1. The survey map of NEP-Wide. The green squares (square $\sim 10' \times 10'$) represent the FOV of individual exposures of IRC. The NEP-Deep exposures are shown as red squares. In addition, we also show the FOVs of CFHT optical survey as two large red boxes.

CFHT's MegaPrime wide field camera (see Hwang et al. 2007). We used the CFHT data for the purpose of identification of sources found in the NEP-Wide survey. The rest of the NEP-Wide area was observed by the 1.5 m telescope at Maidanak Observatory in Uzbekistan under very good seeing conditions ($\lesssim 1''$) with Johnson's B, R, and I filters. The result of the Maidanak optical survey will be published elsewhere, but we have utilized both CFHT and Maidanak data for the purpose of identification of the infrared selected sources.

The purpose of this paper is to present the basic strategies of the NEP-Wide survey and the properties of the sources found from it. More detailed analysis of the sources will be postponed to forthcoming papers. This paper is organized as follows. In the next section, we describe survey strategy, and the data reduction process. In section 3, we present the characteristics, and nature of the detected sources. We then present the number count band in section 4 and summarize our results in the final section.

2. NEP-Wide Survey and Data Reduction

2.1. Survey Strategies

The large area of ~ 5 degree^2 of the NEP-Wide survey was required to avoid uncertainty of cosmic variance in the universe at $z = 0.5$–1, to search for the large-scale fluctuations of the cosmic near infrared (NIR) background, and to obtain a large sample of ultra-luminous infrared galaxies. In order to cover such a large area with small FOV ($10' \times 10'$) of IRC for extragalactic study, NEP is the most suitable area because another high visibility area of South Eclipic Pole (SEP) region lies very close to the Large Magellanic Cloud and the visibility is not sufficiently high at any other places.

There were strong constraints on making a large area map using IRC. First, the FOV of the MIR-L (long wavelengths of MIR) channel is separated by approximately $20'$ from that of the NIR and MIR-S (short wavelength of MIR) channels of AKARI/IRC, although the three channels take images simultaneously. Second, the position angle of IRC FOVs depends on the date of the observation because the sun-shield of the AKARI satellite always has to point to the Sun and thus the focal plane instruments are aligned along ecliptic coordinates.

Given these constraints, to maximize the survey efficiency toward the NEP we planned to make seven concentric circles (and one additional in some quadrants) centered on NEP with the FOVs of all IRC channels. The survey was scheduled to be completed within a year (see figure 1). Also shown in this figure are the NEP-Deep exposure map indicated by red boxes as well as the optical survey area of CFHT as two large red boxes. For the observational redundancy, an observation on a circle was planned to be shifted with half of FOVs of neighboring observations, so that any area would be observed at least twice. Each pointing observation was done by the 'IRC03' template. This observing mode was designed for general purpose imaging observations that take images with three filters in a pointed observation. For each filter two imaging observations are made with dithering operations. The detailed observational procedure for each Astronomical Observation Template (AOT) is described in AKARI IRC Data User Manual.[1]

[1] ⟨http://www.ir.isas.jaxa.jp/AKARI/Observation/#IDUM⟩.

Table 1. Width (FWHM) in units of pixel (and in arcseconds in parentheses) of the Point Spread Function.

	N2	*N3*	*N4*	*S7*	*S9W*	*S11*	*L15*	*L18W*
Single frame	2.9 (4.″2)	2.9 (4.″2)	2.9(4.″2)	2.2 (5.″1)	2.4 (5.″1)	2.4 (5.″1)	2.3 (5.″6)	2.3(5.″6)
Mosaic	3.8 (5.″5)	4.1 (6.″0)	4.1 (6.″0)	2.5 (5.″9)	2.8 (6.″6)	2.5 (5.″9)	2.5 (6.″2)	2.5 (6.″2)

Table 2. Integration time and number of exposures.*

	N2	*N3*	*N4*	*S7*	*S9W*	*S11*	*L15*	*L18W*
Integration time per exposure	44.4	44.4	44.4	16.36	16.36	16.36	16.36	16.36
Number of exposures	3	3	2	9	9	6	9	9
Integration time per pointing	133.2	133.2	88.8	147.24	147.24	98.16	147.24	147.24

* Time is in units of second.

The observations were carried out as planned as long as the schedule permits. The NEP-Wide survey was completed with 446 pointing observations.

2.2. *Pre-Processing*

The observed data were processed using IRC data reduction pipeline version 071017. The pipeline subtracts the dark current, normalizes the signal, corrects for the linearity, and applies the flat field corrections. The cosmic rays are removed in the pipeline for the MIR images (*S7*, *S9W*, *S11*, *L15*, and *L18W*) during the image stacking process because these images are taken with multiple exposures per pointing. However, the number of exposures for NIR bands was smaller than that of MIR bands, and therefore the cosmic rays have not been completely removed during the stacking of multiple exposure images. Especially, there are only two frames to be stacked in most of the *N4* data so that the majority of cosmic rays remain unremoved. In such cases, we have applied a program L.A. cosmic (van Dokkum 2001) which employs Laplacian edge detection algorithm. The cosmic ray removal for *N4* band image data heavily relied on L.A. cosmic task which often makes somewhat erroneous corrections for the cosmic ray effects. Therefore we should take the *N4* band photometric data with more care than those of other wavelengths. We applied L.A. cosmic for *N2* and *N3* as well. For these data, large fraction of cosmic rays can be removed during the stacking process.

Finally the astrometric information is added. The astrometric solution can be found nearly automatically for *N2*, *N3*, *N4*, *S7*, and *S9W* images by comparing with the 2MASS database. However, the mid-infrared band frames for *S11* to *L24* contain relatively smaller numbers of sources so that often automatic astrometric solution cannot be derived. In such cases, we have used imaging data with astrometric solutions at shorter wavelengths in order to obtain the accurate positional information for next longer wavelength images (i.e., *S9W* for *S11*, etc). This procedure provides reasonable results up to *L18W* images for most exposures. However, the procedure was successful for only 239 frames out of 446 for *L24* band due to a small number of identifiable sources. Because of such a poor astrometric calibration we do not present the analysis of the *L24* band data in this study. We will report the result for *L24* band in forthcoming papers.

After the astrometric solutions are settled for individual pointing data, we mosaicked them to produce a single master image of entire survey region for each passband using SWarp software package by E. Bertin at Terafix.[2]

The procedure to obtain photometric data is described in next subsection. Note that magnitude system referred henceforth is AB magnitudes.

2.3. *Point Spread Function*

In order to check the quality of the mosaic images, we have measured the FWHM of bright point sources in mosaic images and listed the results in table 1, together with single frame FWHMs taken from IRC Data User Manual.[1] In the case of NIR bands, the mosaic images have about 30% larger FWHM than single frame values while the degradations in *S* and *L* bands are much smaller. The degradation in NIR bands is mostly due to the elongated shape of PSFs in NIR bands.

2.4. *Coverage and Noise Maps*

Since the survey was carried out with multiple, but non-uniform number of pointings, the integration time varies over the survey region. The number of pointings ranges from 1 to 3 and most regions are covered twice. The integration times per pointing are listed in table 2. The actual integration time for given line of sight can be obtained by multiplying the single pointing integration time in table 2 with the number of pointings of that direction. Single pointing integration varies from 89 (*N4*) to 147 s (*S7*, *S9W*, *L15*, and *L18W*). The noise levels depend on the total integration time. Figure 2 shows the coverage map of *S11*, as an example, which corresponds to the distribution of integration time over the survey region.

We also estimated the noise levels throughout the survey area by measuring the *rms* fluctuations, using 16×16 nearby pixels centered on each pixel. The poorly covered regions are expected to have large *rms* fluctuations while well sampled regions have small fluctuations. Most regions have *rms* fluctuations less than 6 ADU s^{-1} which corresponds to point source detection limit (5-σ) of 19-th magnitude. The very noisy region shown in the right hand side of the *rms* map was exposed only once, and therefore we were not able to properly remove cosmic rays.

[2] See ⟨http://terapix.iap.fr/IMG/pdf/swarp.pdf⟩ for the detailed description of this software.

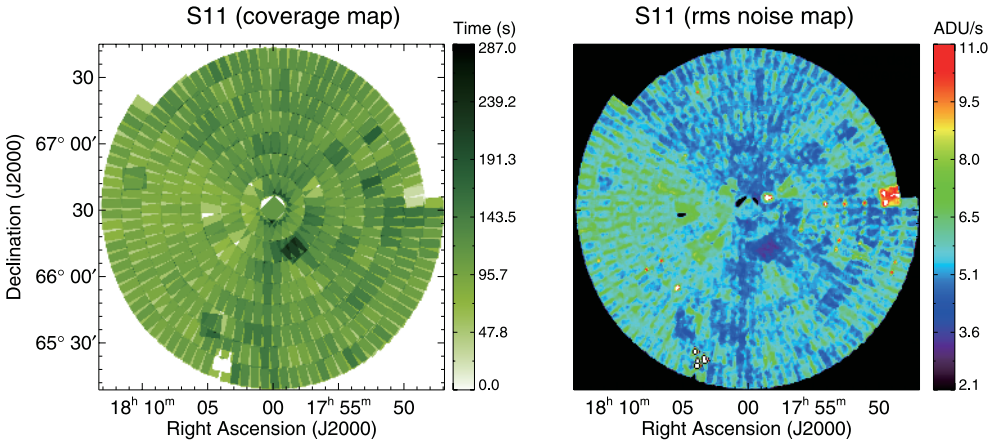

Fig. 2. The coverage map which is analogous to the map of integration times, of NEP-Wide survey at *S11* band (left panel) and noise map (right panel).

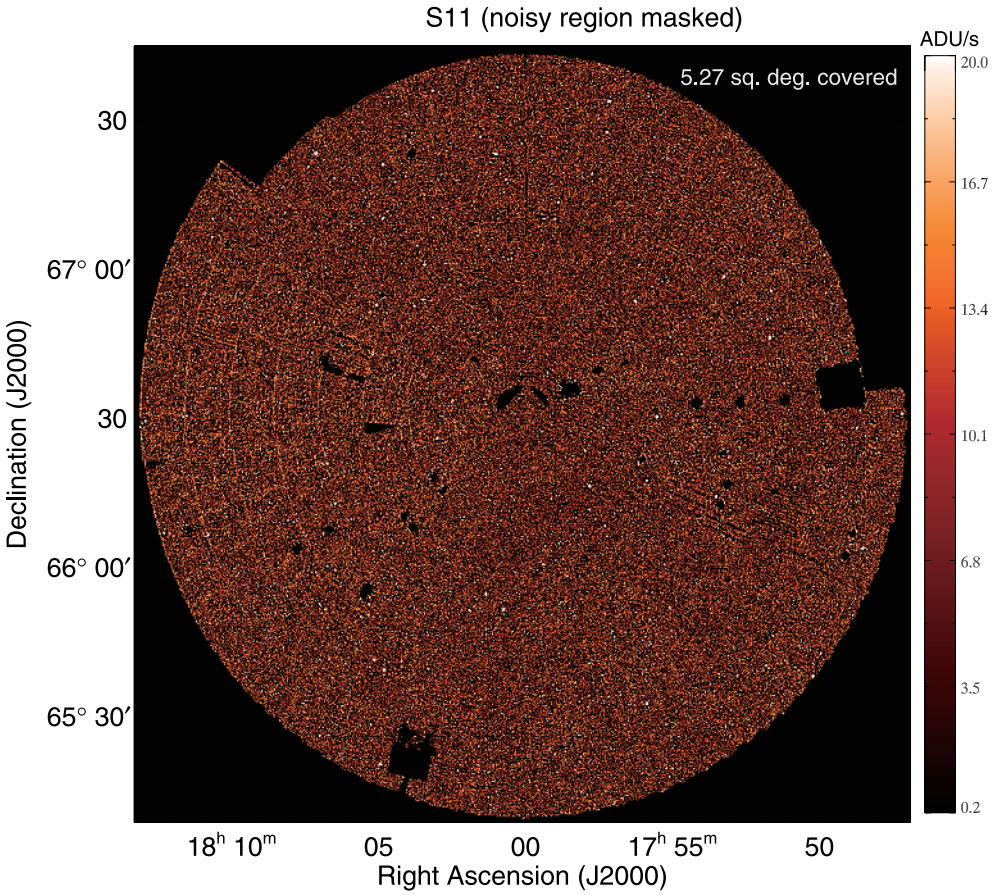

Fig. 3. The *S11* band image map of the survey area excluding the high noise region.

We found that a sector at RA $= 17^{\rm h}50^{\rm m}$ and Dec $= 66°35'$ in the figure 2 has systematically higher noise levels. The AKARI has suffered from the Earth shine problem during the summer of 2007 when more stray light entered the focal plane. The data obtained during this period show systematically higher background level in all filter bands. The higher background level means higher Poisson noise, and such an effect is shown in the *rms* map of figure 2.

After making the noise map, we produced a low-noise maps excluding high noise regions in order to avoid too many false detections. In figure 3, we show an example of *S11* band image with *rms* fluctuations smaller than 6 ADU s^{-1}.

The photometry was done using this low-noise map. The total area of *S11* map was 5.35 degree^2 and the area excluded due to high noise level is around 0.12 degree^2 leaving 5.23 degree^2 of low-noise region.

Table 3. 5σ detection limits and numbers of sources detected over 3σ threshold for 8 filter bands.

	N2	*N3*	*N4*	*S7*	*S9W*	*S11*	*L15*	*L18W*
5σ detection limit (AB magnitude)	21.5	21.8	21.7	19.5	19.4	18.9	18.5	18.7
Number of detected sources	92731	104014	98704	14545	18366	15561	11713	14087

2.5. *Photometry*

We used SExtractor (Bertin & Arnouts 1996) to detect the sources in the individual image of each band. We have confirmed a source if it has more than five contiguous pixels above 3 times of *rms* fluctuations of the sky. The intensity of each source was measured within the isophotal aperture that satisfies the criteria for the source detection. The photometry was done using SExtractor in single mode.

The detection limits depend on the noise levels which vary from place to place. Since the low-noise map shown in figure 3 covers the region with *rms* fluctuation less than $6\,\mathrm{ADU\,s^{-1}}$, the 5-σ detection limit should be better than 19-th magnitude at 11 μm. The resulting average 5-σ detection limits for eight photometric bands are listed in table 3, together with the number of sources detected over 3-σ detection threshold.

The numbers of sources detected in individual filters vary significantly. There are much more sources in near infrared than mid infrared. For example, there are about 104000 sources in *N3* band while about 14500 sources are detected in *S7*.

2.6. *Astrometric Accuracy*

In order to check the accuracy of our astrometric solutions, we compared the positional data of AKARI's point sources that are brighter than 19-th magnitude in *N2* and 18-th magnitude in *S11*, with the counterpart sources in CFHT data. For this purposes, we matched our source list with that of the CFHT data base by Hwang et al. (2007). The matching radius was chosen to be 3.″5 and the number of matched sources was about 2000. The astrometric comparison is shown in figure 4. We found that there is an offset of $\Delta(\cos\delta \times \alpha) = 0.''33$ and $\Delta\delta = -0.''2$ between CFHT and NEP-Wide astrometric solutions (AKARI − CFHT). This offset is known to exist when CFHT data were compared with Guide Star Catalogue (GSC: Jenkner et al. 1990). The *rms* deviations shown in the figure is about 1.″38 which is about 30% of the FWHM of the single frame PSF of the NIR bands.

2.7. *Photometric Consistency*

In order to check the accuracy of our photometry, we compared our catalogue with that of NEP-Deep field by Wada et al. (2008) in figure 5. The NEP-Deep field lies within the NEP-Wide survey area as shown in figure 1. We found that the scatter is becomes larger at fainter magnitudes, and there exist small but non-negligible difference (order of 0.02–0.06 magnitudes) between NEP-Wide and NEP-Deep in the sense that NEP-Wide is slightly fainter. When checked with the Monitor Field data by Takagi et al. (2007), we found opposite tendency, although the difference is also very small. The systematic difference may have resulted from the different photometry parameters. The small differences of $\lesssim 0.06$ magnitude would not affect our conclusions of the present work of characterization of the data and source.

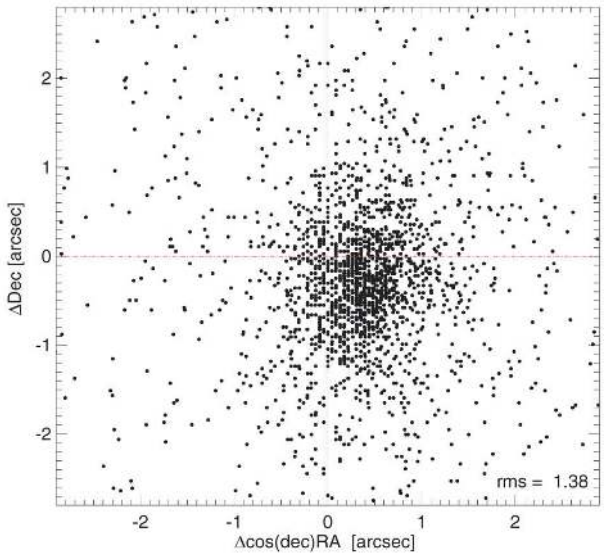

Fig. 4. The scatter diagram of astronometric positions between the NEP-Wide data and the CFHT. We found that there is an offset between CFHT and NEP-Wide astrometric solutions of about 0.″39. The *rms* deviations shown in the figure is about 1.″38 which is about 30% of the FWHM of the single frame PSF of the NIR bands of AKARI.

3. Nature of the Detected Sources

The sources detected in our survey ranges from various Galactic objects to distant galaxies and quasars. Although it is not easy to identify the nature of all the sources using the AKARI data alone, we try to categorize them based on our photometric data and optical survey data. It is worth noting that the previous study by Lee et al. (2007) for the early data of NEP-Deep showed that the majority of the *S11* flux limited sample are star forming galaxies while less than 20% of the detected sources are found to be stars. Since the NEP-Wide survey has a sensitivity similar to that of the sample discussed in Lee et al. (2007), we also expect a large fraction of the mid-infrared selected sample to be star forming galaxies.

In order to distinguish objects with different natures, we generated color–magnitude (CM) and color–color (CC) diagrams for the sources that are matched with the CFHT point sources. In figure 6, we show the CM diagrams of NEP-Wide sources with *S11* brighter than 18.5 magnitude. The red dots represent the sources whose stellarity parameters (*sgc*) are greater than 0.8 in the CFHT r'-band image and r' magnitude brighter than 19. These sources are thought to be mostly stars,

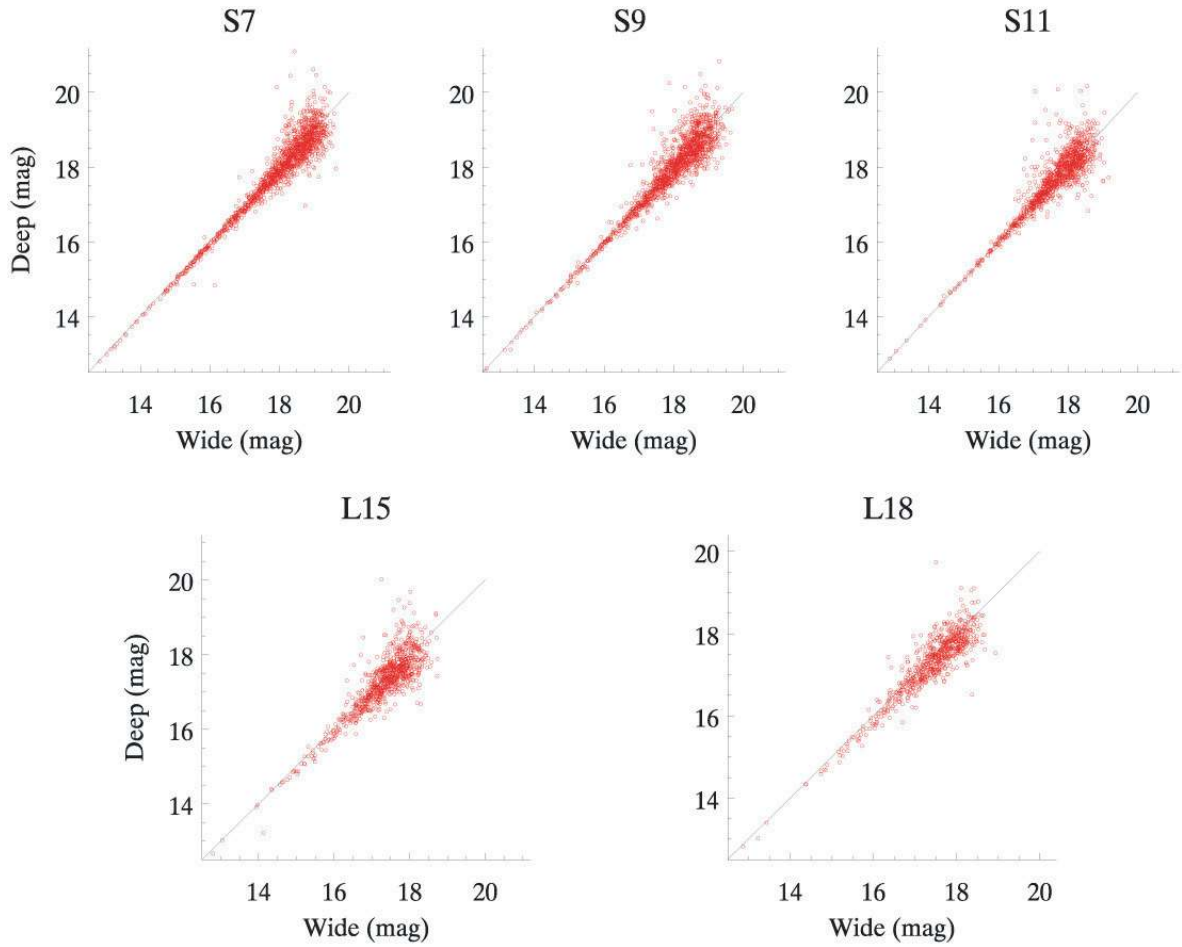

Fig. 5. The comparisons of the photometric magnitudes between the NEP-Deep data by Wada et al. (2008) and the NEP-Wide data of the present work for N- and S-bands. There are small but non-negligible systematic differences between these two data sets. NEP-Wide is fainter by about 0.02–0.06 magnitude.

and we have confirmed that the optical–IR spectral energy distribution (SED) of these objects indeed closely follow that of black body, assuring that these are stars. As expected from the black body nature of stellar SEDs, the star-like sources have NIR colors lying in rather narrow ranges in $N2-N4$ and $N3-N4$. The number of sources with $S11 < 18.5$, $sgc > 0.8$, and $r' < 19$ are 780 while total $S11$ flux limited sample within the CFHT survey field is 3800. This means that the stellar fraction is about 20% for a sample with $S11 < 18.5$. The r' brightness cut was applied to avoid possible contamination by faint galaxies. This can be compared with the previous study by Lee et al. (2007) who found that the stellar fraction is about 18% of the 72 $S11$ flux limited sample after careful examination of optical to MIR SEDs as well as the optical images. Thus our criteria of $sgc > 0.8$ for bright optical sources can detect all the stars and could possibly include some distant compact galaxies.

Also shown in these CM diagrams are the tracks of star forming galaxies represented by M 82 (violet lines) and M 51 (blue lines) SEDs. We have taken the template SEDs of these star forming galaxies from Silva et al. (1998). These galaxies are taken as typical examples of different star formation rates (SFR): M 51 for low SFR and M 82 for moderate SFR galaxies. Although the rest frame near infrared color depends on the star formation rate significantly, the tracks converge into nearly identical lines at redshifts greater than 0.5. Since we assumed the luminosity to be L_*, the tracks of galaxies with different luminosities would slide horizontally from the lines shown in this figure so that the sources at lower right corner can also be explained by fainter star forming galaxies lying at moderate redshifts ($z \lesssim 1.0$).

In figure 7, we show near and mid infrared CC diagrams. The red dots are the 'stellar sources' as defined by the stellarity parameter for bright optical sources. As expected from the narrow ranges in $N2-N3$ and $N3-N4$ colors, majority of the stellar sources lie in a small blue box shown in the left panel. The tracks of star forming galaxies are also shown in these CC diagrams. Here we have added Arp 220 which is a typical example of starburst galaxy. While the tracks are highly degenerated in the NIR CC diagram in the left panel, the MIR−NIR CC diagram shown in the right panel is more sensitive to the star formation rates as well as the redshifts. For the galaxies with very high star formation rates (e.g., Arp 220),

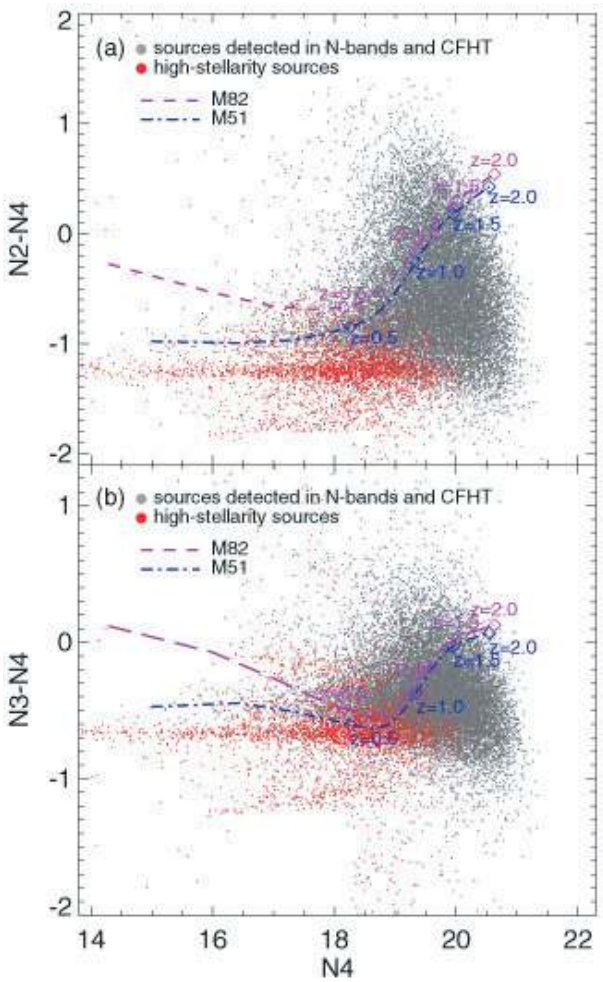

Fig. 6. The *N4* versus *N2−N4*, and *N4* versus *N3−N4* CM diagrams for the sources that have optical counterparts within 3.″5 in the CFHT survey data by Hwang et al. (2007), and *S11* magnitude brighter than 18.5. The red dots represent the sources whose r' stellarity greater than 0.8 and r' magnitudes brighter than 19. Also shown here are the tracks of star forming galaxies as represented by template SEDs of M 51 and M 82 by Silva et al. (1998).

rest frame $S7-S11$ color is very blue because of very strong 7.7 μm PAH feature. However as this PAH feature redshifts to 11 μm band, the tendency of the color is reversed. As seen in the right panel of the figure 7, redder part of the $S7-S11$ color is occupied by the galaxies with higher star formation rate located at ($z \lesssim 1.0$).

In figure 8, we have shown two more CC diagrams with MIR ($S7-S11$ or $L15-L18W$) and NIR colors ($N2-N4$). The upper panel shows the CC diagram of $N2-N4$ versus $L15-L18W$ while the lower panel show the CC diagram of $S7-S11$ versus $L15-L18W$. The tracks of three types of star forming galaxies represented by M 51, M 82, and Arp 220.

Again we find that the NEP sources occupy large area in these CC diagrams. When compared with the tracks of various types of star forming galaxies, we find that majority of NEP sources are star forming galaxies within moderate redshifts. However, we also notice that many sources fall on some parts of CC plane which cannot be occupied by star forming galaxies such as lower left part and lower right of the *N2−N4* versus *L15−L18W* CC diagram. Also the rare objects with very red *N2−N4* color are likely to be AGNs (Lee et al. 2007). The range of *L15−L18W* color range of the NEP-Wide sources appears to be much wider than typical star forming galaxies. Unlike *S7−S11*, *L15−L18W* color does not seem to be an indicator of SFR. Clearly more careful study is needed to identify the nature of the sources found in the NEP-Wide survey.

We attempted to identify MIR sources among the radio emitting objects from the NRAO/VLA Sky Survey (NVSS) data (Condon et al. 1998). Out of about 260 radio sources brighter than 2.5 mJy at 1.4 GHz (21 cm) in NEP-Wide area, we found 30 sources that match with the MIR source at 15 μm. In figure 9 we show the optical–MIR SED plots of the 10 sources which have optical counterparts in CFHT or Maidanak data. The radio flux is shown as a blue square in the righthand side of each plot. Although there appears no clear correlation between MIR and radio fluxes, we found that the large fraction of the radio sources with MIR counterparts are suspected to be AGNs. For example, 3 out of 10 ($\sim$30%) sources show power-law SEDs (J180900.83+670425.0, J180034.67+673615.9, and J175104.17+660649.5), indicating they are indeed AGNs. This can be compared with the finding by Lee et al. (2007) that only 6% of the MIR selected sources are AGNs. The remaining 7 sources which show NIR bumps need more careful examination since some of them could also be AGNs having large amount of late type stars.

It is important to distinguish between stellar and extended sources for further analysis. As we saw in the comparison with the NEP-Early data, almost all the sources with stellarity $sgc > 0.8$ are likely to be stars. We estimated the fraction of stars among the mid-infrared (MIR) sources by using the CFHT data. We identified the sources as stars when the mid-infrared sources have optical counterparts with high stellarity parameter (i.e., $sgc > 0.8$) in the CFHT field. The 'stellar fractions' determined in this way in *S9W*, *S11*, *L15*, and *L18W* band sources are shown in figure 10 as a function of magnitude. The size of the magnitude bin was 0.5 mag. In *S9W* and *S11*, the stellar fraction is very large for bright sources and decreases rapidly toward the fainter ends. However, the stellar fraction of the sources detected in *L15* and *L18W* are much smaller than that of *S11*, and it decreases rather slowly toward the fainter parts. There is virtually no sources with high stellarity among faint sources.

4. Flux Distribution in Mid Infrared

One of the powerful ways for the study of the evolution of galaxies is to examine the distribution of sources as a function of flux. We know that the source counts flatten at faint flux but the magnitude of the counts provides a strong constraint on source count models by constraining the local luminosity function such as L_* and ϕ of the Schechter luminosity function since different assumptions on these parameters can produce very different normalizations. For observed source counts, in particular at 15 μm we will be able to confirm which of the ELAIS fields (ELAIS N or S) is giving us the right picture since the ELAIS S field has a much lower normalization (Gruppioni et al. 2002). In order to do this, we need to accurately separate

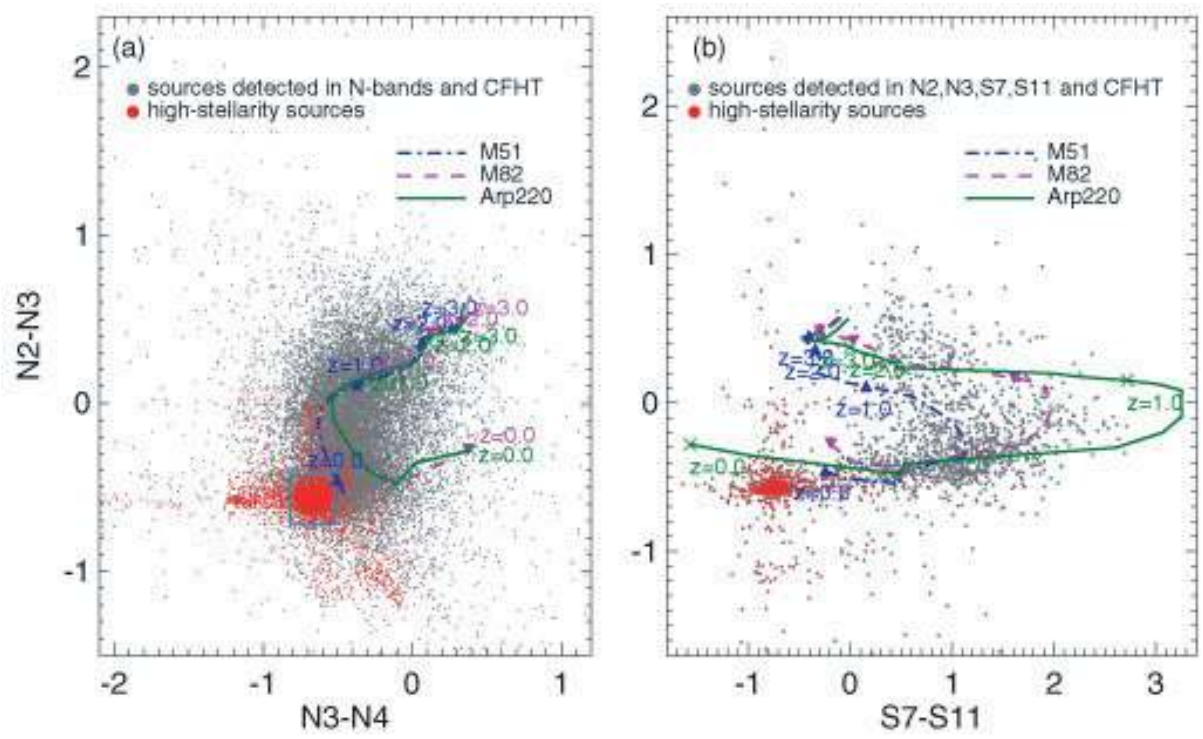

Fig. 7. The $N2-N3$ versus $N3-N4$ and $N2-N3$ versus $S7-S11$ CC diagrams for the same sources shown in figure 6. The symbols are the same as those in figure 6.

the galaxies and stars, estimate the incompleteness, and assess effects of saturation for bright sources, among others. Also, a combination of NEP-Deep and NEP-Wide data is necessary for more accurate source count over wide range of fluxes.

We, therefore, leave such tasks for subsequent works. Instead of showing differential count in a more accurate way, we simply show the histograms of the NEP-Wide sources detected in *S9W*, *S11*, *L15*, and *L18W* in figure 11. The expected slope for uniform source distribution in Euclidean geometry is also shown in this histograms.

For the case of *S9W* and *S11*, we have shown both the raw counts without taking out stars, as well as the count for the non-stellar objects (i.e., galaxies) by statistically correcting for stellar sources using the stellar fraction of figure 10. Since the stellar fractions in *L15* and *L18W* are relatively small, the correction does not make any significantly different histogram.

We find that the slopes of the number distribution for *L15* and *L18W* sources are close to that of uniform distribution in Euclidean space (i.e., 0.6) while the raw data of *S9W* and *S11* show slightly less steep distribution. However, the flux distribution for non-stellar sources after correcting for stellar fraction becomes more consistent with the uniform source distribution, although the actual slopes in these passbands are still slightly flatter than *L15* and *L18W* bands.

Such a difference might be attributed to strong positive K-corrections from the 7.7 μm feature and 11.3 μm (in the *S11* band) PAH features. These features will be local at the brightest magnitudes and the decrease in slope seen at fainter magnitudes could be caused by these emission features leaving the pass bands. This would also lead to a non-Euclidean slope

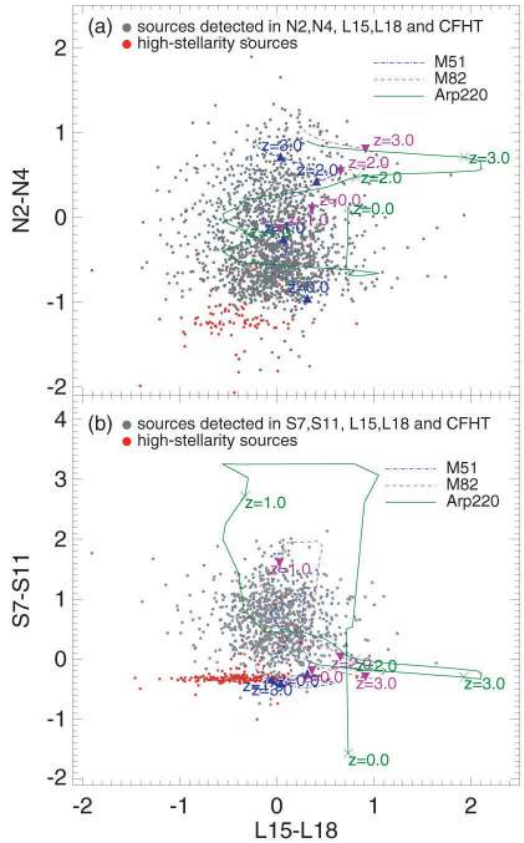

Fig. 8. The $S7-S11$ versus $L15-L18W$ CC diagrams for the same sources shown in figure 7.

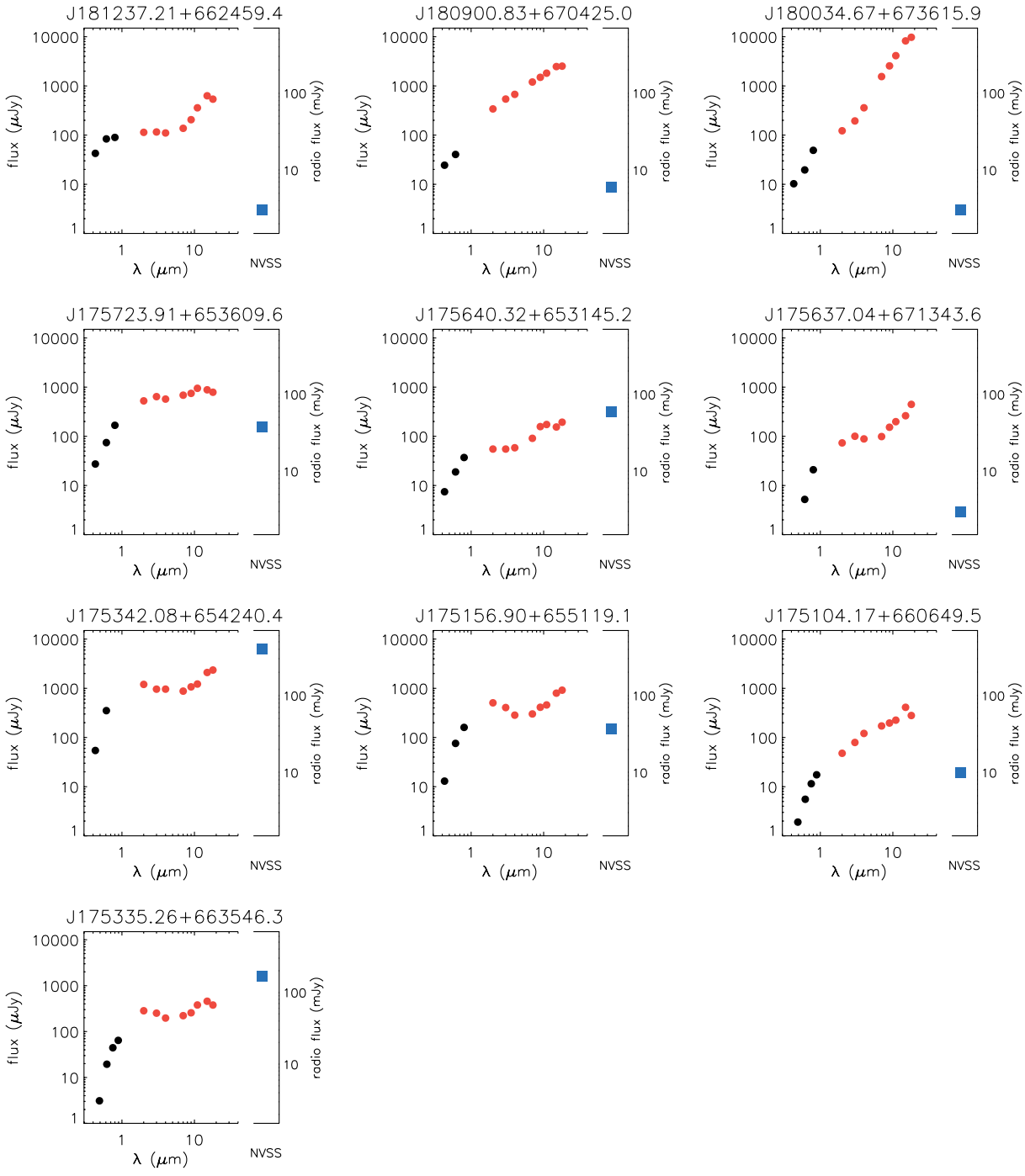

Fig. 9. Optical–MIR SED plots for the radio sources with MIR and optical counterparts. The radio fluxes at 1.4 GHz are indicated as blue squares. Four objects show clear power-law behavior of the AGNs. There are also several sources which show NIR bumps indicating the presence of late type stars. These objects need more careful examination, but some of them could also be AGNs.

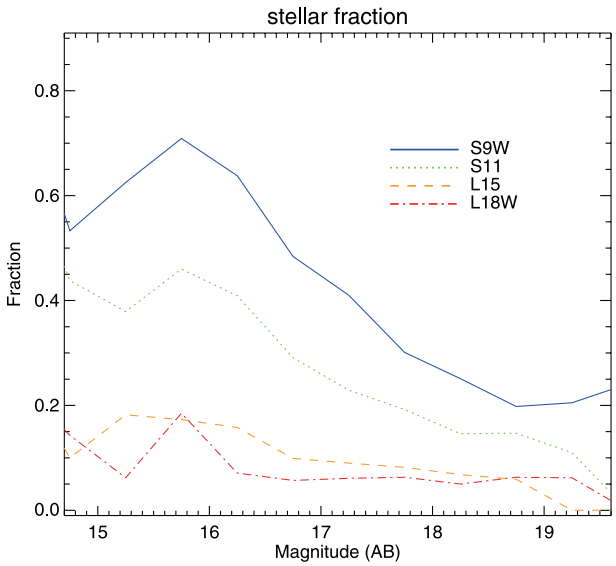

Fig. 10. The fraction of stellar sources in MIR band sources as a function of the MIR magnitudes. The sources in *S9W* and *S11* bands contain many stars, but the stellar fraction becomes much smaller for *L15* and *L18W* bands. Also, the stellar fraction decreases toward the fainter ends in all bands.

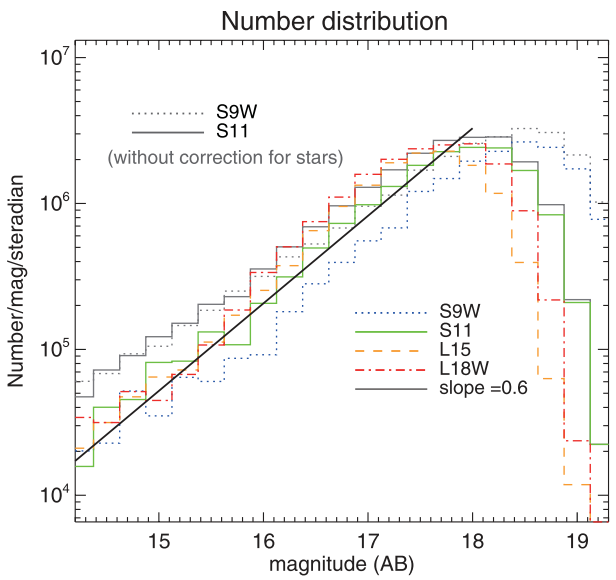

Fig. 11. The histogram of MIR sources in NEP-Wide survey for *S9W*, *S11*, *L15*, and *L18W* bands. The slopes for *L15* and *L18W* at brighter end are close to 0.6, as expected for uniform distribution in Euclidean space. The count plots after correcting for the stars (i.e., applying the fraction of non-stellar objects) are also shown for the cases of *S9W* and *S11* since the stellar fractions in these bands are significant and have strong dependence on magnitude. The corrected counts are consistent with the uniform source distribution in flat universe.

at bright magnitudes in the short wavelength counts. The *L15* and *L18W* band counts generally sample the higher redshift universe and are not so affected by local contributions.

Note that a similar effect was observed in the IRAC 8 μm band which straddled the 7.7 μm emission feature.

5. Summary

The NEP-Wide survey of AKARI covered about 5.8 degree^2 region centered on NEP. The survey data consisting of 446 pointing observations at 8 band filters from 2 to 18 μm are reduced. Total number of sources detected at least in one filter band reaches about 104000. However, the numbers of sources at MIR passbands are significantly smaller than those at NIR. The 5-σ detection limits are typically about $21\overset{\mathrm{m}}{.}5$ at 2–5 μm bands, 18.5 to $19\overset{\mathrm{m}}{.}5$ for 7 to 18 μm bands. Our data will be complemented by the NEP-Deep survey data which are deeper than NEP-Wide with smaller areal coverage.

We used the CFHT optical data which covered 2 degree^2 within the NEP-Wide survey area to identify the nature of the objects. In particular, we have used the stellarity parameter of SExtractor to distinguish between stars and non-stellar objects which are mostly external galaxies.

The majority of MIR sources are thought to be star forming galaxies at redshift $\lesssim 1$, while stars comprise around 10%–20%. The shorter wavelength band (9 and 11 μm) sources contain more stars than longer wavelength bands (15 and 18 μm) in MIR.

The color–color diagrams at near and mid infrareds show broader distribution in color–color space while stars are known to exist in narrow areas in these diagrams. In particular, $N2-N4$ versus $N3-N4$ CC diagram is found to be very useful in identifying stars as the stars have narrow ranges of these colors.

The CC diagrams can also be used to identify galaxy types. For example, AGN can be distinguished from relatively red $N2-N4$ color ($\gtrsim 1.5$), while starburst galaxies show very red $S7-S11$ colors (>3). The $S7-S11$ color appears to be a good indicator for star formation rates.

We have shown the histograms in magnitudes for *S9W*, *S11*, *L15*, and *L18W* bands. The detailed shapes of the histograms depend on the pass band, but *S9W* and *S11* have less steep slope than *L15* and *L18W* at bright ends (brighter than 18 magnitude). Such a difference have been caused by the contamination of stars for shorter wavelength bands, but strong positive K-correction from the 7.7 and 11.3 μm PAH features may also be partially responsible. The *L15* and *L18W* band source distribution is consistent with that of uniform sources in flat universe. However, the detailed shape at faint part should be sensitive to the luminosity and number density evolution of star forming galaxies.

This work was supported by KRF grant No. 2006-341-C00018. This work is based on observations with AKARI, a JAXA project with the participation of ESA. M.G.L and M.I were supported in part by a grant (R01-2007-000-20336-0) from the Basic Research Program of the Korea Science and Engineering Foundation.

References

Bertin, E., & Arnouts, S. 1996, A&AS, 117, 393
Condon, J. J., Cotton, W. D., Greisen, E. W., Yin, Q. F., Perley, R. A., Taylor, G. B., & Broderick, J. J. 1998, AJ, 115, 1693
Gruppioni, C., Lari, C., Pozzi, F., Zamorani, G., Franceschini, A., Oliver, S., Rowan-Robinson, M., & Serjeant, S. 2002, MNRAS, 335, 831
Hwang, N., et al. 2007, ApJS, 172, 583
Jenkner, H., Lasker, B. M., Sturch, C. R., McLean, B. J., Shara, M. M., & Russell, J. L. 1990, AJ, 99, 2082
Lee, H. M., et al. 2007, PASJ, 59, S529
Matsuhara, H., et al. 2006, PASJ, 58, 673
Matsuhara, H., et al. 2007, PASJ, 59, S543
Murakami, H., et al. 2007, PASJ, 59, S369
Onaka, T., et al. 2007, PASJ, 59, S401
Silva, L., Granato, G. L., Bressan, A., & Danese, L. 1998, ApJ, 509, 103
Takagi, T., et al. 2007, PASJ, 59, S557
van Dokkum, P. G. 2001, PASP, 113, 1420
Wada, T., et al. 2008, PASJ, 60, S517